THE JOURNAL OF PHYSICAL CHEMISTRY C

pubs.acs.org/JPCC Article

Probing the Reaction Zone of Nanolaminates at ~μs Time and ~μm Spatial Resolution

Haiyang Wang, Baptiste Julien, Dylan J. Kline, Zaira Alibay, Miles C. Rehwoldt, Carole Rossi, and Michael R. Zachariah*

Cite This: J. Phys. Chem. C 2020, 124, 13679−13687 Read Online

ACCESS | Metrics & More | Article Recommendations | Supporting Information

ABSTRACT: Reactive nanolaminates are a high-energy-density configuration for energetics that have been widely studied for their tunable energy release rates. In this study, we characterized Al/CuO nanolaminate reactions with different fuel/oxidizer ratios and bilayer thicknesses using both macro- and microscale high-speed imaging/pyrometry. Under microscopic imaging, we observe significant corrugation (the ratio of the total geometrical length of the flame to the width of the sample in the direction perpendicular to propagation) of the flame, which can increase the reaction surface area by as much as a factor of 3. This in turn manifests itself as an increase in the global burn rate (total nanolaminate film length/total burn time). We find that the global burn rate can be predicted as the product of the microburn rate (local vector burn rate at the microscopic scale) and the corrugation. These corrugation effects primarily impact fuel-rich conditions, resulting in higher global burn rates. We find that the reaction zone has a thickness of ~150 μm. Finally, we present a 3D rendering of what we believe the reaction zone looks like, based on the results from *in-operando* observation and SEM cross-sectional imaging.

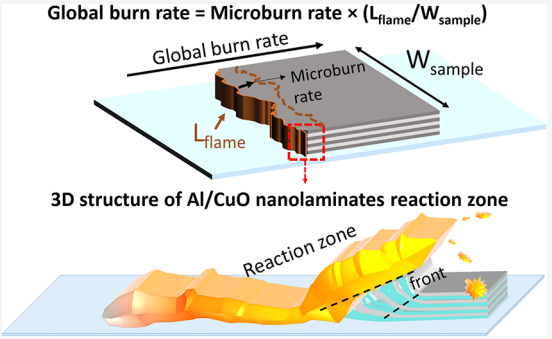

1. INTRODUCTION

Employing nanomaterials in thermites increases the interfacial surface area between the fuel and oxidizer and thus decreases the diffusion distances, resulting in faster reactions and energy release rates. Using nanomaterials in energetics has increased burn rates from mm/s to m/s and even km/s in some cases.[1−10] To obtain a high interfacial contact area between the fuel and oxidizer, different approaches such as ultrasonication,[11] electrospraying/electrospinning,[12−14] mechanical milling,[15−17] self-assembly (static electricity-based,[18] ligand-based,[3,19] sol−gel synthesis,[20] DNA-based assembly),[21,22] and recently 3D printing[23−29] have been explored with varying levels of success. An alternative approach to creating high-density, high interface surface area composites in thermites is by fabrication of nanolaminate structures through physical vapor deposition (PVD). Thermite nanolaminates offer a highly controllable architecture and have been incorporated into a variety of micro-pyrotechnic devices commonly used in micro-electromechanical systems (MEMS).[30−35] In addition to thermites, this configuration has also been explored in binary reactive multilayers such as Al/Ni,[36,37] Al/Zr,[38] and Al/Pt.[39]

Al/CuO nanolaminates have drawn particular attention due to their high reactivity and gas generation ability.[31,34,40−42] The effects of different parameters of the layered Al/CuO systems with respect to bilayer thicknesses,[31,34] equivalence ratios,[43] interfacial layers (insertion of another layer between Al and CuO),[44−46] sample width,[32,33,47] and oxidation state (using Cu_2O or CuO) have been studied.[48] The ignition temperatures/delays, burn rates, and thermal decomposition properties have also been characterized on the macroscopic scale.[31−34,40−42,47] However, there is limited literature on the microscopic characterization of the reaction. While most of these studies have focused on gasless self-propagating high-temperature synthesis (SHS) systems such as Al/Ni nanolaminates,[37,49−51] few efforts have focused on thermites.[52]

Herein, we employed a recently developed microscopic dynamic imaging system to probe the reaction zone of Al/CuO nanolaminates on a time and length scale comparable to the reaction front dimensions and time scales. Microscopic imaging utilizes μs and μm temporal and spatial resolution, respectively, and is capable of being used as a pyrometer.[52,53] By employing this technique, we obtained unprecedented images and temperature profiles across the reaction zone that enabled us to demonstrate, for the first time, the effect of the corrugation of the flame front on the global burn rate of thermite nanolaminates. Quenched SEM imaging is addition-

Received: February 25, 2020
Revised: May 21, 2020
Published: May 26, 2020

https://dx.doi.org/10.1021/acs.jpcc.0c01647
J. Phys. Chem. C 2020, 124, 13679−13687

ally used to correlate observation of the fast video imaging and the microstructure pre- and postcombustion.

2. EXPERIMENTAL SECTION

2.1. Methods and Materials. Al/CuO nanolaminates with dimensions of ~30 mm (length) × 4 mm (width) were sputter-deposited onto a ~31.75 mm (length) × 17.75 mm (width) × 500 μm (thick) glass slide (Figure S1). Titanium filaments (100 μm width) were patterned at both ends underneath the nanolaminate line to resistively heat the multilayer to its ignition point (Figure S1). Different configurations of Al/CuO nanolaminates with three equivalence ratios (Ø, defined as the ratio of the actual fuel/oxide ratio to the stoichiometric fuel/oxide ratio) were fabricated: (1) 15 bilayers of Al/CuO of 100/200 nm (Ø 1); (2) 11 bilayers of Al/CuO of 200/200 nm (Ø 2); and (3) 9 bilayers of Al/CuO 300/200 nm (Ø 3). To minimize the number of variables, all of the laminates were fabricated to a total thickness of ~4.5 μm. The details of the magnetron sputtering of Al/CuO nanolaminates can be found in previous studies,[31,34] and typical cross-sectional images are shown in Figure 1. Each sample is characterized by the Al to CuO

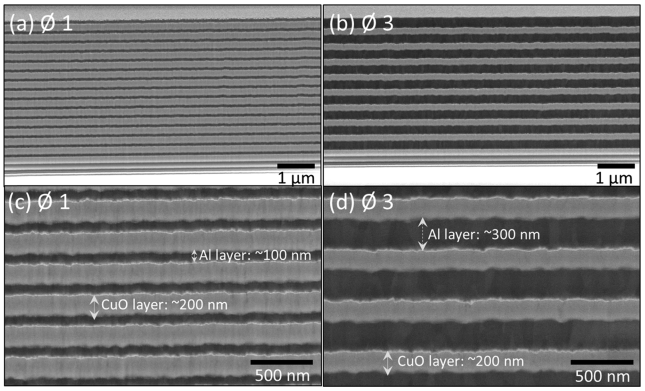

Figure 1. Low- (a, b) and high-resolution (c, d) SEM images of cross-sectional Al/CuO nanolaminates with equivalence ratios of 1 (a, c) and 3 (b, d).

equivalence ratio (Ø). Note that in a Ø = 1 sample, the aluminum thickness is half the CuO thickness (stoichiometric stack), whereas Ø > 1 corresponds to a fuel-rich situation with thicker aluminum layers. The thickness accuracy of sputtering is 10%. For instance, the CuO layer thickness is 200 ± 20 nm and Al layer thickness is 100 ± 10, 200 ± 20, and 300 ± 30 nm for Ø 1, 2, and 3 samples, respectively. Furthermore, Ø 2 Al/CuO nanolaminates with different bilayer thicknesses (thickness of a single layer of Al and CuO) were fabricated to investigate the microburn (defined later) rate differences. All of the configurations used in this study are summarized in Table 1.

2.2. Microscopic and Macroscopic Imaging. The setup used in this study is shown in Figure 2. The glass slides coated with Al/CuO nanolaminates were mounted on a three-axis translational stage in between two camera systems with different imaging length scales. On the far side, a macroscopic imaging high-speed camera (Phantom V12.1) captures the front side of the burning event (unless otherwise noted) at a resolution of 640 × 200 pixels (~78 μm/pixel) and a sample rate of 13 000 frames per second (Figure 2a). The aperture was nominally f22, with a 2−6 μs exposure. The near-side microscopic imaging system (Figure 2b, microscopic imaging) images the backside of the sample through the transparent glass slide (unless otherwise noted). The microscopic imaging system employs a high-speed camera (Phantom VEO710L) coupled to a long working distance microscope lens (Infinity Photo-Optical Model K2 DistaMax, CF-4 Objective), which provides a pixel/distance ratio of ~1.7 μm/pixel (256 × 256 pixels) from a working distance of ~54 mm. High-speed microscopy videos were recorded at a sample rate of 60 000 frames per second with an exposure of 15 μs. Ignition of the nanolaminates was achieved by applying a direct current pulse (~500 ms duration and ~1.8 A) through the embedded thin titanium line (Figure S1). Propagation is mirrored between the two cameras; in the microscopic direction, the propagation direction is from left to right, while the macroscopic view captures propagation from right to left. To account for this, the images captured by the macroscopic camera are horizontally flipped in the article so that propagation appears to be in the same direction for both cameras (Figure 2a-2).

From the macroscopic and microscopic videos, the global burn rate (Figure 2a-3) and microburn rate (Figure 2b-3) can be obtained, respectively. The global burn rate (Figure 2a-3) is defined as the total nanolaminate film length/total burn time. This is the nominal burn rate that is quoted in papers. The microburn rate is determined under microscopic imaging and is measured using custom software that has been previously reported by Kline et al.[54] In particular, for two consecutive frames (Figure 2b-3, frames 1 and 2), we took each of the points in the flame front in frame 1 and matched it to the closest point in the flame front in frame 2, calculated the distance between the two points, and then divided that distance by the time per frame (1/fps) to get the local velocity. A detailed diagram and typical results (Figure S2) demonstrate how the microburn rate was obtained.

Both the high-speed macroscopic and microscopic apparatuses were calibrated for color pyrometry to estimate the flame temperature of the reaction. The details of color pyrometry can be found in previous studies.[52,53] Briefly, three-channel intensity (RGB: red, green, and blue) ratios are extracted to represent the reaction flame temperature after calibration with a blackbody source (Mikron M390). Raw videos, such as in Figure 2a-1,b-1, are processed using a home-built MATLAB routine and built-in MATLAB demosaicing algorithms with

Table 1. Configurations of Al/CuO Nanolaminates[a]

Ø	bilayers	bilayer thickness (nm)	thickness of a single Al layer (nm)	thickness of a single CuO layer (nm)	Ø	bilayers	bilayer thickness (nm)	thickness of a single Al layer (nm)	thickness of a single CuO layer (nm)
1	15	300	100	200	2	10	440	220	220
2	11	400	200	200	2	15	300	150	150
3	9	500	300	200	2	20	230	115	115

[a]Total thickness fixed at ~4.5 μm.

https://dx.doi.org/10.1021/acs.jpcc.0c01647
J. Phys. Chem. C 2020, 124, 13679−13687

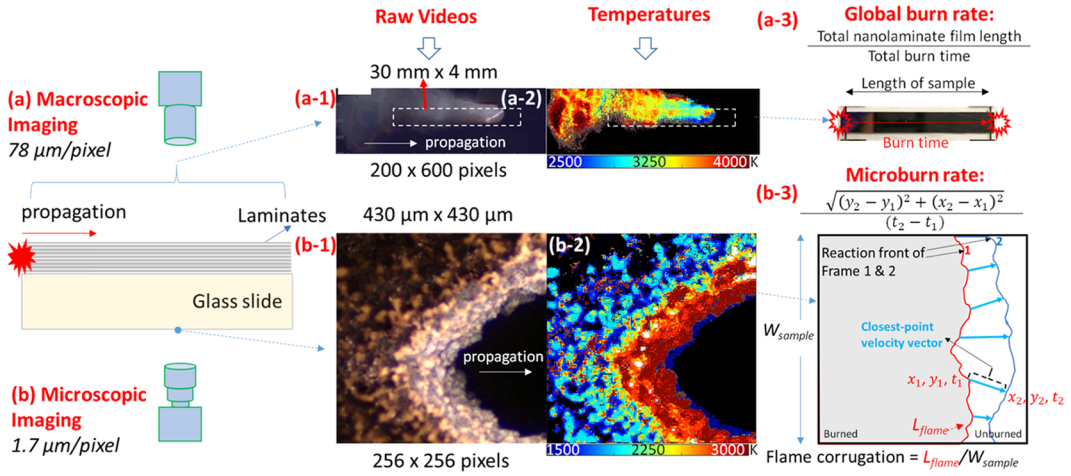

Figure 2. Schematic of experimental configuration and macroscopic (a) and microscopic (b) imaging of Al/CuO nanolaminates burning on a glass slide. Typical snapshots from raw videos (a-1, b-1) and corresponding temperature maps (a-2, b-2) from macroscopic imaging (a-1, a-2) and microscopic imaging (b-1, b-2).

respect to the camera's Bayer filter. Corresponding flame temperature maps were output and reported as exemplified by Figure 2a-2,b-2. The error threshold of measured flame temperatures is roughly 200−300 K. The flame temperatures were averaged based on all available points throughout the whole burning event and utilized for experimental calculations.

2.3. SEM and EDS. Al/CuO nanolaminates were first examined using a focused-ion beam FIB-SEM FEI Helios NanoLab DualBeam. The images were obtained using a backscattered electron detector to achieve good contrast (Figure 1). The postcombustion products and quenched nanolaminates were characterized by scanning electron microscopy (SEM, NNS450) and energy-dispersive X-ray spectroscopy (EDX, ThermoFisher Scientific, formerly FEI/Philips). The working distance is 5 mm with an in-lens SE/BSE detector (TLD) and an accelerating voltage of 20 kV. For topside SEM imaging, the glass slide was placed on the SEM stage aided by a carton tape with the nanolaminate side pointed upwards. Very small areas (<0.5 mm^2) of unburnt materials were found at the end corners of the laminate samples, as labeled in Figure S1. Quenching of the flame in these areas is likely due to the additional heat loss to the titanium filament and glass substrate. The SEM imaging of the cross-sectional view of the quenched sample was carried out by having the glass slide sectioned in liquid nitrogen and attached to the side of the SEM stage with nanolaminates facing outward. The glass slides with combustion products were sputter-coated with a Pt/Pd layer on both sides before conducting SEM/EDS to avoid electron charge build up and obtain better images.

3. RESULTS AND DISCUSSION

3.1. Global Burn Rate and Flame Temperature. Figure 3a−c shows examples of macroscopic burning snapshots of the samples at various equivalence ratios and their respective average flame temperatures. From the array of macroscopic snapshots, one can obtain the global burn rate. We use the term "macroscopic" in this paper to distinguish the images obtained from those at the microscopic view (defined as a view when the resolution is ∼1.7 μm/pixel). For the Ø 1 case, the global burn rate is 5.4 ± 0.7 m/s with an average flame temperature of ∼3300 K. At Ø 2, both the burn rate and flame

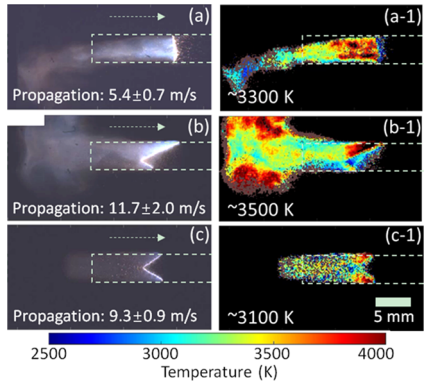

Figure 3. Macroscopic burning snapshots (a−c) and the corresponding flame temperature maps (a-1−c-1) of Al/CuO nanolaminates with equivalence ratios of 1 (a), 2 (b), and 3 (c). Note: The brightness and contrast in (a−c) were adjusted in postprocessing to show the whole flame with gas ejection.

temperature are the highest of the three samples studied—11.7 ± 2.0 m/s and 3500 K. At Ø 3, the burn rate declines slightly to 9.3 ± 0.9 m/s; however, the flame temperature reduced to ∼3100, ∼200 K less than that of the Ø 1 case. Previous studies also show that the Ø 2 case has a significantly higher burn rate compared to the stoichiometric case[31,34,43] and that the fuel-rich sample released more heat compared to Ø 1 based on differential thermal analysis.[43]

3.2. Microscopic Imaging: Microburn Rate and Flame Corrugation. While a flame front of a thermite reaction may appear planar under a macroscopic (normal) view, it may appear quite different under a microscopic observation. When observed at a temporal and spatial resolution of $\sim 10^{-1}$ s and ∼0.1 mm, respectively, it has been shown that many other heterogeneous systems (e.g., Ti−C, Ni−Al) exhibit a planar combustion wave; however, at higher resolutions, the propagation appears to be much more discrete with deviations from a unimodal velocity distribution and nonuniform temperature distributions along the reaction front.[48−55]

We now turn our attention to a more microscopic view with a resolution of ∼1.7 μm/pixel to probe the reaction zone in greater detail and compare how propagation at this scale compares with observations at the macroscale. Ultimately,

https://dx.doi.org/10.1021/acs.jpcc.0c01647
J. Phys. Chem. C 2020, 124, 13679−13687

observations at the microscale must lead to explaining and be consistent with resulting phenomena that are seen at the macroscale. Initial observations reveal that measured microburn rates (local vector burn rate at the microscopic scale, details could be found in Figure S2) are lower than the corresponding global burn rates. Similar to studies on other heterogeneous systems,[48−55] we find that the flame front is not planar but corrugated. The microscopic snapshots of the three samples at selected times are shown in Figure 4a−c. Also

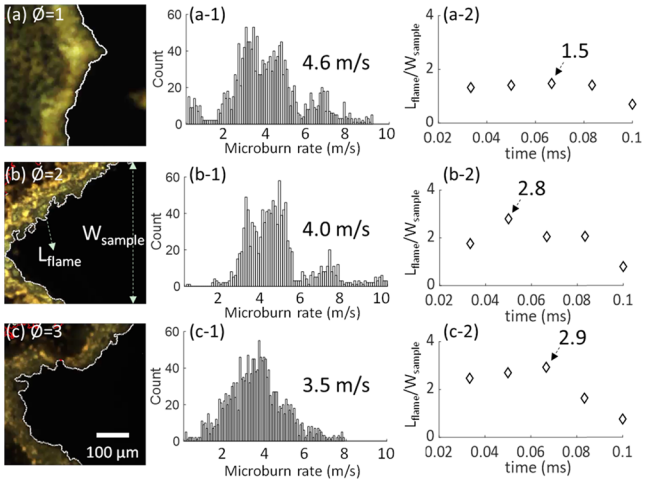

Figure 4. Microscopic imaging snapshots (a−c), microburn rate velocity distribution (a-1−c-1); flame corrugation (a-2−c-2) of nanolaminates with equivalence ratios ø 1 (a), 2 (b), and 3 (c). Propagation is from left to right. Note: One might find that we used the highest value for the corrugation data (a-2−c-2), that is, because only in these corresponding frames was the whole flame length captured.

shown are the microburn rate distributions and the extent of the flame corrugation as defined by the ratio of the total geometrical length of the flame (L_{flame}) to the width of the sample in the direction perpendicular to propagation (W_{sample}) (Figure 4b).[54] If the flame front were planar, this ratio would be unity. The average microburn rates based on the histogram for ø 1, 2, and 3 are 4.6, 4.0, and 3.5 m/s, respectively. One thing that immediately stands out is that, for the two fuel-rich cases, the microburn rates are significantly slower than the global burn rates of 11.7 ± 2.0 and 9.3 ± 0.9 m/s. This can be explained by the extent of flame corrugation (L_{flame}/W_{sample}) at the microscopic scale. The measured corrugations of the flame front for the fuel-rich cases are 2.8 (ø 2) and 2.9 (ø 3) at the microscale, roughly two times higher than that of the stoichiometric case (1.5). Data on this behavior is presented in Figure 4.

With respect to the fuel-rich cases, the higher corrugation of the flame enables a larger burning surface area and thus has a higher global burn rate.[56,57] Quantitatively, we should expect then that the global burn rate should be equal to the product to the microburn rate and the flame corrugation as shown in the following equation1

$$\text{global burn rate} = \text{microburn rate} \times \left(\frac{L_{flame}}{W_{sample}}\right) \quad (1)$$

where L_{flame} represents the measured length of the flame and W_{sample} represents the observable sample width in the microscopy image (~430 μm).

The results of this analysis are summarized in Table 2. At first glance, one can see that eq 1 does a reasonable job of capturing how the effects of the microburn rate and flame corrugation operate in conjunction, though it is not perfect. In fact, given the width and shape of the velocity distribution functions shown in Figure 4 and the fact that eq 1 provides the right ordering in the global burn rate, this implies that the system operates on mean properties and not the tails of the distribution function. In other words, for a system with the same chemistry, corrugating the flame front will enhance the global burn rate (in principle). This principle is similar to voids in a propellant that can be used to accelerate a flame by enhancing the reaction surface area and modes of heat transfer.[58]

Laminar flame theory[59] says that for a planar reaction front, the propagation velocity is proportional to the square root of the product of the thermal diffusivity (α) and reaction rate (r). Thus, for a small segment of the flame front, the microburn rate can be estimated according to eq 2. Since we could not obtain an absolute value for the reaction rate, the calculated microburn rates are presented as normalized values for a comparison between different laminate configurations.

$$\text{calculated microburn rate} \sim (\alpha \times r)^{1/2} \quad (2)$$

We can approximate the reaction rate, r, as a normalized value using a contact area in equation3

$$r \sim k\cdot[\text{Al}]^n\cdot[\text{CuO}]^m \sim k \times (\text{contact area between Al and CuO}) \quad (3)$$

where k is the reaction rate constant. [Al] and [CuO] are the reactant concentrations of Al and CuO, with n and m representing the reaction orders of Al and CuO, respectively, which nominally are not known.

Since both fuel (Al) and oxidizer (CuO) in the chemical reaction are in the solid state, we simplify the calculation using the contact area between the two to represent the reactant concentration. For simplicity, we also assume that the activation energy (E_a) is insensitive to the equivalence

Table 2. Summary of Global Burn Rate, Microburn Rate, Flame Corrugation, Thermal Diffusivity, Flame Temperature, and Comparison to eqs 1 and 2

Ø	measured global burn rate (m/s)	measured microburn rate (m/s)	measured corrugation $\left(\frac{L_{flame}}{W_{sample}}\right)$	expected global burn rate from eq 1 (m/s)	calculated thermal diffusivity (m^2/s)	calculated contact area (normalized)	calculated microburn rate (normalized) from eq 2 (m/s)	measured reaction zone (μm)
1	5.4 ± 0.7	4.6	1.5	6.9	1.5×10^{-5}	1	1	170
2	11.7 ± 2.0	4.0	2.8	11.2	2×10^{-5}	0.72	0.98	150
3	9.3 ± 0.9	3.5	2.9	10.1	2.4×10^{-5}	0.59	0.97	150

https://dx.doi.org/10.1021/acs.jpcc.0c01647
J. Phys. Chem. C 2020, 124, 13679−13687

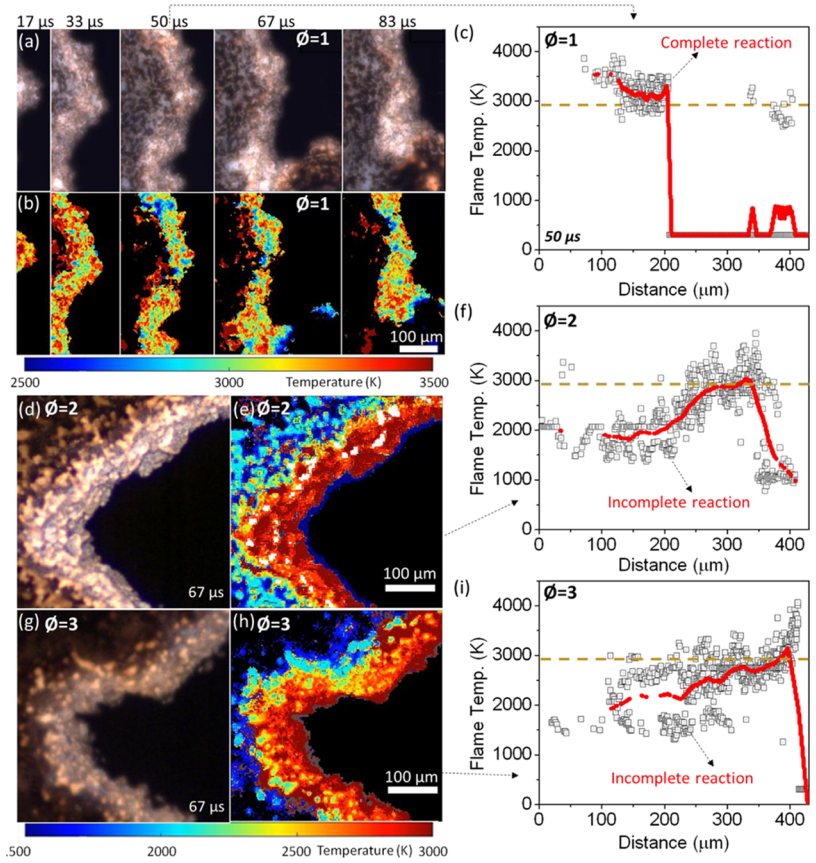

Figure 5. Microscopic imaging snapshots (a, d, and g), temperature maps (b, e, and h), and temperature profiles (c, f, and i) of the reaction zone of Al/CuO nanolaminates with ⌀ 1 (a–c), ⌀ 2 (d–f), and ⌀ 3 (g–i). Note: The data is a summary of five different positions (heights) in the images. Details of the data point locations can be found in Figures S8–S11. Propagation is from left to right.

ratio;[60] therefore, k is essentially constant and is presented as a normalized value (see justification in Table S1). The reaction rate constant is assumed to follow Arrhenius behavior as represented in the following equation4

$$k = Ae^{-E_a/RT} \tag{4}$$

where A is the pre-exponential factor, E_a is the activation energy (kJ/mol), T is the average flame temperature (K), and R is the gas constant (J/mol·K).

For evaluation of eq 2, we note that the thermal diffusivity of aluminum ($\sim 1 \times 10^{-4}$ m^2/s) is more than 10 times higher than that of CuO ($\sim 1 \times 10^{-5}$ m^2/s).[31] The fuel-rich cases of ⌀ 2 (Al layer: 200 nm) and ⌀ 3 (Al layer: 300 nm) have 2× and 3× thicker aluminum layers than the stoichiometric case (Al layer: 100 nm). Therefore, the thermal diffusivities for the samples are estimated to be ranked as ⌀ 3 (2.4×10^{-5} m^2/s) > ⌀ 2 (2×10^{-5} m^2/s) > ⌀ 1 (1.5×10^{-5} m^2/s) (see Table 2 and details in Table S1).

The bilayer thickness of nanolaminates determines the rate of intermixing between reactants and is critical for burn rate control.[30−48,61] The contact area between Al and CuO layers is simply proportional to the (number of bilayers × 2 − 1) and represented as a normalized value in Table 2. Using eq 2, the calculated microburn rate (normalized) shown in Table 2 indicates that the equivalence ratio does not play a significant role in propagation. We note however that while eq 2 shows only a 3% difference between ⌀ 1 and ⌀ 3, the experiments indicate a 24% difference (4.6 vs 3.5 m/s). This likely represents the inherent difficulty in predicting flame propagation in nonhomogeneous materials with high degrees of flame front corrugations. In short, the experimental behavior is not quasihomogeneous, even though the structures shown in Figure 1 would suggest perhaps otherwise.

To further assess these results, the Ø 2 case was tested with three different bilayer thicknesses: 10 bilayers (440 nm bilayer thickness), 15 bilayers (300 nm bilayer thickness), and 20 bilayers (230 nm bilayer thickness) (see Figures S3–S5). We observe increasing microburn rates of ∼3, ∼4.5, and ∼5.0 m/s for the 10-, 15-, and 20-bilayer samples, respectively, which match well with our calculations (Table S2), indicating that the contact between the fuel and oxidizer plays a significant role in the chemistry at the microscale. The corrugation of the flame is measured to be ∼1.8, ∼2.3, and ∼3.3, which correspondingly gives the calculated global burn rates of ∼5 (Figure S3), ∼10 (Figure S4), and ∼16 m/s (Figure S5). These results match well with the measured global burn rates of ∼4.9 ± 0.1, ∼10.3 ± 0.3, and 16.9 ± 0.1 m/s, respectively, which further confirms the proposal of eq 1.

We can conclude that changes in the global burn rate are almost exclusively due to the corrugation of the reaction front. There is also likely an additional heat transfer mechanism that may be in play since the fuel-rich cases are also affected by the corrugation. Under fuel-rich conditions, excess Al will melt and can result in nonuniform heating that increases corrugation of the reaction front[56] (more ejected particles could be found in fuel-rich samples; details in Supporting Information Videos). Combustion residues collected postburning shown in Figure S6 confirm that the fuel-rich cases have significantly higher

https://dx.doi.org/10.1021/acs.jpcc.0c01647
J. Phys. Chem. C 2020, 124, 13679−13687

number of particles than the stoichiometric case. This point is further discussed with the SEM imaging of the reaction zone (Section 3.4).

3.3. Microscopic Imaging of the Reaction Zone with Pyrometry. Detailed microscopic snapshots and the corresponding temperature maps are summarized in Figure 5. Herein, the "reaction zone" is defined as the zone where the reaction occurs at temperatures near the adiabatic flame temperature of Al/CuO (~2840 K).[13,34,52,56] To get an idea of the reaction zone width, we transformed the colored microscopic snapshots into black/white images to outline the reaction zone area (Figure S7). The width of the reaction zone can be obtained by dividing the area by the flame length (flame lengths were obtained from data in Figure 5). According to the calculations, the reaction zone width of Al/CuO ⌀ 1 is ~170 and ~150 μm for both ⌀ 2 and ⌀ 3 (Table 2).

From the stoichiometric ratio case shown in Figure 5a and the corresponding temperature maps outlined in Figure 5b, one can see that the reaction zone is at high temperatures of ~3000 K and above. The postcombustion products rapidly cool to below our measurement range (<1000 K) and are shown as black areas in Figure 5. Temperatures across the reaction zone are plotted and summarized in Figure 5c (⌀ 1). The demonstrated temperature profiles are at the 50 μs time frame after triggering the ignition. For the ⌀ 1 case, we note that the data points confirm that the temperatures achieved by the reaction are close to the adiabatic flame temperature, implying a complete reaction.

For the fuel-rich cases, such as ⌀ 2 (Figure 5d–f), the temperature gradient is shallower and drops off past the flame front. This behavior is more pronounced for ⌀ 3 and can be attributed to further mixing of excess fuel acting as both a heat sink and as an enhanced thermal diffuser, particularly when melted.

It is notable that the flame temperature we obtained in the reaction zone is close to or above the adiabatic flame temperature of Al/CuO (~2840 K). These "super-adiabatic peaks" may correspond to rapid chemistry within the nanolaminates followed by relatively slow heat dissipation into the neighboring unburnt material regions until further "ignition." This so-called discrete combustion was reviewed in detail in ref 55.

From the temperature profiles, we can get a rough idea that the reaction front thickness (defined as the width of the temperature profile to reach the maximum temperature) gets thicker as the equivalence ratio increases (⌀ 2 and ⌀ 3). However, since the estimated reaction front thickness (1–5 μm, see Table S1) is at the limit of our current resolution (~2 μm/pixel), we will reserve more detailed studies on the reaction front structure for the future.

3.4. Electron Microscopy: Constructing a 3D Structure of the Reaction Zone. To further reveal the reaction zone structure, a typical combustion event is illustrated in Figure 6a. A quenched corner (Figure S1) of the ⌀ 1 sample was characterized by SEM/EDS. Figure 6b,c shows top-view SEM and EDS images of the quenched surface of stoichiometric (⌀ 1) Al/CuO nanolaminates. Figure 6b has been labeled to show the various regions that can be observed including the reacted residue, the unreacted nanolaminate surface, and the corrugated area between them (marked blue) that outlines the quenched reaction zone. The main point of this figure is for the reader to note that the width of the labeled reaction zone (~100–200 μm) is consistent with what is

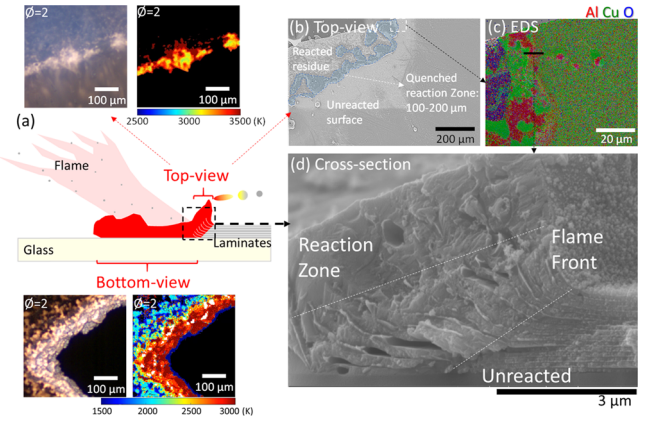

Figure 6. Cartoon (a) of the reaction zone of Al/CuO nanolaminates based on in-operando and SEM imaging. SEM (b) and EDS images (c) of the quenched surface of Al/CuO nanolaminates (⌀ 1). Cross-sectional SEM view (d) of the quenched reaction front. Propagation is from left to right. Inset in (a) is the top-view and bottom-view of the burning Al/CuO nanolaminates with equivalence ratios of 2.

observed in the microscopy images of the propagating reaction (Figure 5).

By sectioning the quenched sample in liquid nitrogen, we can image the quenched reaction zone (Figure 6d). The image clearly shows the region of unreacted nanolaminates, the reaction zone, and the reaction flame front in a 3D structure (more details can be found in Figure S12). As seen in the quenched reaction front (Figure 6d) and illustrated in Figure 6a, the nanolaminates swell when heated and exhibit some curvature as a result. The reaction occurs in a thin area of ~2–5 μm (reaction front), but the reaction products are rapidly ejected into a much larger area of the ~100–200 μm reaction zone.

The curving and swelling behavior may be due to the melting and decomposition of Al and CuO, which is controlled by the rapid heat transfer. The thickness of the reaction flame front, Δx, can be roughly estimated from a heat flux calculation[31,34,37] (see Table S1 for details), as shown in the following equation5

$$\Delta x = \frac{\lambda}{\rho C_p v} \tag{5}$$

where λ is the thermal conductivity (W/(m·K)), ρ is the density (kg/m^3), C_p is the heat capacity (J/(kg·K)), and v is the reaction velocity (m/s).

This simple heat flux-based calculation gives a reaction front thickness of ~2–3 μm, which is comparable to what we see in the SEM (Figure 6d) and in the temperature profiles (Figure 5). Using this calculated reaction front thickness, we can estimate the heat flux for each equivalence ratio (eq 5 in the Supporting information), ⌀ 2 (1.2×10^{11} W/m^2) > ⌀ 3 (9.6×10^{10} W/m^2) > ⌀ 1 (5.3×10^{10} W/m^2). This order is the same as that seen for the global burn rate. It is noted that these heat flux values are not exact but are reported here to provide a rough idea of orders of magnitude. Based on the heat flux data, one could in principle estimate the reaction time vs heat exchange time and the burn rate, which we will consider in a future work.

The 3D nature of the reaction zone is illustrated in Figure 6a. In particular, a very different view of the reaction zone is seen depending on the view, i.e., top or bottom. The reaction

https://dx.doi.org/10.1021/acs.jpcc.0c01647
J. Phys. Chem. C 2020, 124, 13679–13687

zone observed from the top-view (top insets in Figure 6a) is much thinner compared to the bottom-view (~60 vs ~150 μm), while the whole top-view reaction zone is at a temperature >3000 K, further confirming the 3D structure of the reaction zone (more information in Figure S13).

4. CONCLUSIONS

In this study, we explored the reaction zone of nanolaminate thermites using both macro- and microscale high-speed videography for imaging/pyrometry at various equivalence ratios. Under microscopic imaging, we observed corrugation of the reaction front, which serves to increase the burn surface area and thus increases the global burn rate. We found that the global burn rate can be modeled as the product of the microburn rate and the corrugation of the reaction front. Corrugation effects impact fuel-rich conditions more, resulting in higher global burn rates compared to the stoichiometric case. We also found that the microburn rate increases with a decrease of bilayer thickness. The reaction zone is found to be ~150 μm wide.

■ ASSOCIATED CONTENT

Supporting Information

The Supporting Information is available free of charge at https://pubs.acs.org/doi/10.1021/acs.jpcc.0c01647.

The macroscopic and microscopic high-speed videos with corrugation and pyrometry results (with different equivalence ratios and different bilayer thicknesses) could be found in the supporting videos (ZIP)

Details on the device and experimental setup; microscopic imaging snapshots of the reaction zone and temperature maps; physical parameters and thermal calculations for Al/CuO nanolaminates with different equivalence ratios; SEM images and EDS maps of quenched Al/CuO nanolaminate surfaces; pictures of combustion residues left on the glass slide after propagation (PDF)

■ AUTHOR INFORMATION

Corresponding Author

Michael R. Zachariah − *University of California, Riverside, California 92521, United States;* orcid.org/0000-0002-4115-3324; Email: mrz@engr.ucr.edu

Authors

Haiyang Wang − *University of California, Riverside, California 92521, United States;* orcid.org/0000-0001-5200-3965

Baptiste Julien − *LAAS-CNRS, University of Toulouse, 31400 Toulouse, France*

Dylan J. Kline − *University of California, Riverside, California 92521, United States; University of Maryland, College Park, Maryland 20742, United States;* orcid.org/0000-0001-8800-2841

Zaira Alibay − *University of California, Riverside, California 92521, United States*

Miles C. Rehwoldt − *University of California, Riverside, California 92521, United States; University of Maryland, College Park, Maryland 20742, United States*

Carole Rossi − *LAAS-CNRS, University of Toulouse, 31400 Toulouse, France;* orcid.org/0000-0003-3864-7574

Complete contact information is available at: https://pubs.acs.org/10.1021/acs.jpcc.0c01647

Notes

The authors declare no competing financial interest.

■ ACKNOWLEDGMENTS

The authors gratefully acknowledge support from the Army Research Office and the Air Force Office of Scientific Research. A part of this work was also supported by the European Research Council under the European Union's Horizon 2020 research and innovation program (grant agreement no. 832889—PyroSafe). Electron microscopy on quenched samples was performed using an FEI NNS450 SEM in the Central Facility for Advanced Microscopy and Microanalysis at the University of California, Riverside. Electron microscopy of as-deposited nanolaminates was performed on SEM FEI Helios NanoLab DualBeam at the Centre de Micro Caractérisation Raymond Castaing (UMS 3623).

■ REFERENCES

(1) Pantoya, M. L.; Granier, J. J. Combustion Behavior of Highly Energetic Thermites: Nano Versus Micron Composites. *Propellants, Explos., Pyrotech.* **2005**, *30*, 53−62.

(2) Moore, K.; Pantoya, M. L.; Son, S. F. Combustion Behaviors Resulting From Bimodal Aluminum Size Distributions in Thermites. *J. Propul. Power* **2007**, *23*, 181−185.

(3) Apperson, S.; Shende, R. V.; Subramanian, S.; Tappmeyer, D.; Gangopadhyay, S.; Chen, Z.; Gangopadhyay, K.; Redner, P.; Nicholich, S.; Kapoor, D. Generation of Fast Propagating Combustion and Shock Waves with Copper Oxide/Aluminum Nanothermite Composites. *Appl. Phys. Lett.* **2007**, *91*, No. 243109.

(4) Shimojo, F.; Nakano, A.; Kalia, R. K.; Vashishta, P. Electronic Processes in Fast Thermite Chemical Reactions: A First-Principles Molecular Dynamics Study. *Phys. Rev. E* **2008**, *77*, No. 066103.

(5) Petrantoni, M.; Rossi, C.; Salvagnac, L.; Conédéra, V.; Estève, A.; Tenailleau, C.; Alphonse, P.; Chabal, Y. J. Multilayered Al/CuO Thermite Formation by Reactive Magnetron Sputtering: Nano Versus Micro. *J. Appl. Phys.* **2010**, *108*, No. 084323.

(6) Weismiller, M. R.; Malchi, J. Y.; Lee, J. G.; Yetter, R. A.; Foley, T. J. Effects of Fuel and Oxidizer Particle Dimensions On the Propagation of Aluminum Containing Thermites. *Proc. Combust. Inst.* **2011**, *33*, 1989−1996.

(7) Zhang, W.; Yin, B.; Shen, R.; Ye, J.; Thomas, J. A.; Chao, Y. Significantly Enhanced Energy Output from 3D Ordered Macroporous Structured Fe_2O_3/Al Nanothermite Film. *ACS Appl. Mater. Interfaces* **2013**, *5*, 239−242.

(8) Becker, C. R.; Apperson, S.; Morris, C. J.; Gangopadhyay, S.; Currano, L. J.; Churaman, W. A.; Stoldt, C. R. Galvanic Porous Silicon Composites for High-Velocity Nanoenergetics. *Nano Lett.* **2011**, *11*, 803−807.

(9) Piekiel, N. W.; Morris, C. J.; Currano, L. J.; Lunking, D. M.; Isaacson, B.; Churaman, W. A. Enhancement of On-Chip Combustion Via Nanoporous Silicon Microchannels. *Combust. Flame* **2014**, *161*, 1417−1424.

(10) Khasainov, B.; Comet, M.; Veyssiere, B.; Spitzer, D. Comparison of Performance of Fast-Reacting Nanothermites and Primary Explosives. *Propellants, Explos., Pyrotech.* **2017**, 754−772.

(11) Sullivan, K.; Zachariah, M. Simultaneous Pressure and Optical Measurements of Nanoaluminum Thermites: Investigating the Reaction Mechanism. *J. Propul. Power* **2010**, *26*, 467−472.

(12) Yan, S.; Jian, G.; Zachariah, M. R. Electrospun Nanofiber-Based Thermite Textiles and their Reactive Properties. *ACS Appl. Mater. Interfaces* **2012**, *4*, 6432−6435.

(13) Wang, H.; Jian, G.; Egan, G. C.; Zachariah, M. R. Assembly and Reactive Properties of Al/CuO Based Nanothermite Microparticles. *Combust. Flame* **2014**, *161*, 2203−2208.

(14) Wang, H.; Jian, G.; Zhou, W.; DeLisio, J. B.; Lee, V. T.; Zachariah, M. R. Metal Iodate-Based Energetic Composites and their

Combustion and Biocidal Performance. *ACS Appl. Mater. Interfaces* **2015**, *7*, 17363−17370.
(15) Stover, A. K.; Krywopusk, N. M.; Gibbins, J. D.; Weihs, T. P. Mechanical Fabrication of Reactive Metal Laminate Powders. *J. Mater. Sci.* **2014**, *49*, 5821−5830.
(16) Guerrero, S. E.; Dreizin, E. L.; Shafirovich, E. Combustion of Thermite Mixtures Based On Mechanically Alloyed Aluminum−Iodine Material. *Combust. Flame* **2016**, 164−166.
(17) Mursalat, M.; Schoenitz, M.; Dreizin, E. L. Effect of Premilling Al and CuO in Acetonitrile On Properties of Al·CuO Thermites Prepared by Arrested Reactive Milling. *Combust. Flame* **2020**, *214*, 57−64.
(18) Kim, S. H.; Zachariah, M. R. Enhancing the Rate of Energy Release from NanoEnergetic Materials by Electrostatically Enhanced Assembly. *Adv. Mater.* **2004**, *16*, 1821−1825.
(19) He, W.; Tao, B.; Yang, Z.; Yang, G.; Guo, X.; Liu, P.; Yan, Q. Mussel-Inspired Polydopamine-Directed Crystal Growth of Core-Shell n-Al@PDA@CuO Metastable Intermixed Composites. *Chem. Eng. J.* **2019**, *369*, 1093−1101.
(20) Gash, A. E.; Satcher, J. H.; Simpson, R. L.; Clapsaddle, B. J. Nanostructured Energetic Materials with Sol-Gel Methods *MRS Proc.* 2003, *800*. 1−12 DOI: 10.1557/PROC-800-AA2.2.
(21) Séverac, F.; Alphonse, P.; Estève, A.; Bancaud, A.; Rossi, C. High-Energy Al/CuO Nanocomposites Obtained by DNA-Directed Assembly. *Adv. Funct. Mater.* **2012**, *22*, 323−329.
(22) Calais, T.; Bancaud, A.; Esteve, A.; Rossi, C. Correlation between DNA Self-Assembly Kinetics, Microstructure, and Thermal Properties of Tunable Highly Energetic Al-CuO Nanocomposites for Micro-Pyrotechnic Applications. *ACS Appl. Nano Mater.* **2018**, 4716−4725.
(23) Murray, A. K.; Isik, T.; Ortalan, V.; Gunduz, I. E.; Son, S. F.; Chiu, G. T. C.; Rhoads, J. F. Two-Component Additive Manufacturing of Nanothermite Structures Via Reactive Inkjet Printing. *J. Appl. Phys.* **2017**, *122*, No. 184901.
(24) Murray, A. K.; Novotny, W. A.; Fleck, T. J.; Gunduz, I. E.; Son, S. F.; Chiu, G. T. C.; Rhoads, J. F. Selectively-Deposited Energetic Materials: A Feasibility Study of the Piezoelectric Inkjet Printing of Nanothermites. *Addit. Manuf.* **2018**, *22*, 69−74.
(25) Mao, Y.; Zhong, L.; Zhou, X.; Zheng, D.; Zhang, X.; Duan, T.; Nie, F.; Gao, B.; Wang, D. 3D Printing of Micro-Architected Al/CuO-Based Nanothermite for Enhanced Combustion Performance. *Adv. Eng. Mater.* **2019**, No. 1900825.
(26) Wainwright, E. R.; Sullivan, K. T.; Grapes, M. D. Designer Direct Ink Write 3D Printed Thermites with Tunable Energy Release Rates. *Adv. Eng. Mater.* **2019**, No. 1901196.
(27) Durban, M. M.; Golobic, A. M.; Bukovsky, E. V.; Gash, A. E.; Sullivan, K. T. Development and Characterization of 3D Printable Thermite Component Materials. *Adv. Mater. Technol.* **2018**, No. 1800120.
(28) Slocik, J. M.; McKenzie, R.; Dennis, P. B.; Naik, R. R. Creation of Energetic Biothermite Inks Using Ferritin Liquid Protein. *Nat. Commun.* **2017**, *8*, No. 15156.
(29) Wang, H.; Shen, J.; Kline, D. J.; Eckman, N.; Agrawal, N. R.; Wu, T.; Wang, P.; Zachariah, M. R. Direct Writing of a 90 Wt% Particle Loading Nanothermite. *Adv. Mater.* **2019**, *31*, No. 1806575.
(30) Egan, G. C.; Mily, E. J.; Maria, J.; Zachariah, M. R. Probing the Reaction Dynamics of Thermite Nanolaminates. *J. Phys. Chem. C* **2015**, *119*, 20401−20408.
(31) Lahiner, G.; Nicollet, A.; Zapata, J.; Marín, L.; Richard, N.; Rouhani, M. D.; Rossi, C.; Estève, A. A Diffusion−Reaction Scheme for Modeling Ignition and Self-Propagating Reactions in Al/CuO Multilayered Thin Films. *J. Appl. Phys.* **2017**, *122*, No. 155105.
(32) Tai, Y.; Xu, J.; Wang, F.; Dai, J.; Zhang, W.; Ye, Y.; Shen, R. Experimental and Modeling Investigation On the Self-Propagating Combustion Behavior of Al-MoO3 Reactive Multilayer Films. *J. Appl. Phys.* **2018**, *123*, No. 235302.
(33) Xu, J.; Shen, Y.; Wang, C.; Dai, J.; Tai, Y.; Ye, Y.; Shen, R.; Wang, H.; Zachariah, M. R. Controlling the Energetic Characteristics of Micro Energy Storage Device by in Situ Deposition Al/MoO3 Nanolaminates with Varying Internal Structure. *Chem. Eng. J.* **2019**, *373*, 345−354.
(34) Rossi, C. Engineering of Al/CuO Reactive Multilayer Thin Films for Tunable Initiation and Actuation. *Propellants, Explos., Pyrotech.* **2019**, *44*, 94−108.
(35) Adams, D. P. Reactive Multilayers Fabricated by Vapor Deposition: A Critical Review. *Thin Solid Films* **2015**, *576*, 98−128.
(36) Grapes, M. D.; Weihs, T. P. Exploring the Reaction Mechanism in Self-Propagating Al/Ni Multilayers by Adding Inert Material. *Combust. Flame* **2016**, *172*, 105−115.
(37) Kim, J. S.; LaGrange, T.; Reed, B. W.; Knepper, R.; Weihs, T. P.; Browning, N. D.; Campbell, G. H. Direct Characterization of Phase Transformations and Morphologies in Moving Reaction Zones in Al/Ni Nanolaminates Using Dynamic Transmission Electron Microscopy. *Acta Mater.* **2011**, *59*, 3571−3580.
(38) Overdeep, K. R.; Schmauss, T. A.; Panigrahi, A.; Weihs, T. P. The Influence of Sample Thickness On the Combustion of Al:Zr and Al-8Mg:Zr Nanolaminate Foils. *Combust. Flame* **2018**, *196*, 88−98.
(39) Abere, M. J.; Yarrington, C. D.; Adams, D. P. Heating Rate Dependent Ignition of Al/Pt Nanolaminates through Pulsed Laser Irradiation. *J. Appl. Phys.* **2018**, *123*, No. 235304.
(40) Abdallah, I.; Zapata, J.; Lahiner, G.; Warot-Fonrose, B.; Cure, J.; Chabal, Y.; Esteve, A.; Rossi, C. Structure and Chemical Characterization at the Atomic Level of Reactions in Al/CuO Multilayers. *ACS Appl. Energy Mater.* **2018**, *1*, 1762−1770.
(41) Zapata, J.; Nicollet, A.; Julien, B.; Lahiner, G.; Esteve, A.; Rossi, C. Self-Propagating Combustion of Sputter-Deposited Al/CuO Nanolaminates. *Combust. Flame* **2019**, *205*, 389−396.
(42) Lahiner, G.; Zappata, J.; Cure, J.; Richard, N.; Djafari-Rouhani, M.; Estève, A.; Rossi, C. A Redox Reaction Model for Self-Heating and Aging Prediction of Al/CuO Multilayers. *Combust. Theory Modell.* **2019**, *23*, 700−715.
(43) Bahrami, M.; Taton, G.; Conédéra, V.; Salvagnac, L.; Tenailleau, C.; Alphonse, P.; Rossi, C. Magnetron Sputtered Al-CuO Nanolaminates: Effect of Stoichiometry and Layers Thickness on Energy Release and Burning Rate. *Propellants, Explos., Pyrotech.* **2014**, *39*, 365−373.
(44) Marín, L.; Nanayakkara, C. E.; Veyan, J.; Warot-Fonrose, B.; Joulie, S.; Esteve, A.; Tenailleau, C.; Chabal, Y. J.; Rossi, C. Enhancing the Reactivity of Al/CuO Nanolaminates by Cu Incorporation at the Interfaces. *ACS Appl. Mater. Interfaces* **2015**, No. 11713.
(45) Marín, L.; Warot-Fonrose, B.; Estève, A.; Chabal, Y. J.; Alfredo Rodriguez, L.; Rossi, C. Self-Organized Al_2Cu Nanocrystals at the Interface of Aluminum-Based Reactive Nanolaminates to Lower Reaction Onset Temperature. *ACS Appl. Mater. Interfaces* **2016**, No. 13104.
(46) Lanthony, C.; Guiltat, M.; Ducéré, J. M.; Verdier, A.; Hémeryck, A.; Djafari-Rouhani, M.; Rossi, C.; Chabal, Y. J.; Estève, A. Elementary Surface Chemistry During CuO/Al Nanolaminate-Thermite Synthesis: Copper and Oxygen Deposition On Aluminum (111) Surfaces. *ACS Appl. Mater. Interfaces* **2014**, No. 15086.
(47) Xu, J.; Tai, Y.; Ru, C.; Dai, J.; Shen, Y.; Ye, Y.; Shen, R.; Fu, S. Characteristic of Energetic Semiconductor Bridge Based On Al/MoOx Energetic Multilayer Nanofilms with Different Modulation Periods. *J. Appl. Phys.* **2017**, *121*, No. 113301.
(48) Blobaum, K. J.; Reiss, M. E.; Plitzko, J. M.; Weihs, T. P. Deposition and Characterization of a Self-Propagating CuO_x/Al Thermite Reaction in a Multilayer Foil Geometry. *J. Appl. Phys.* **2003**, *94*, 2915.
(49) Grapes, M. D.; LaGrange, T.; Woll, K.; Reed, B. W.; Campbell, G. H.; LaVan, D. A.; Weihs, T. P. In Situ Transmission Electron Microscopy Investigation of the Interfacial Reaction Between Ni and Al During Rapid Heating in a Nanocalorimeter. *APL Mater.* **2014**, *2*, No. 116102.
(50) Santala, M. K.; Grapes, M. D.; Weihs, T. P.; Reed, B. W.; LaGrange, T.; Campbell, G. H. Imaging Unsteady Propagation of Reaction Fronts in Reactive Multilayer Foils with Multi-Frame Dynamic TEM. *Microsc. Microanal.* **2014**, *20*, 1584−1585.

(51) Pauls, J. M.; Shuck, C. E.; Genç, A.; Rouvimov, S.; Mukasyan, A. S. In-Situ Transmission Electron Microscopy Determination of Solid-State Diffusion in the Aluminum-Nickel System. *J. Solid State Chem.* **2019**, *276*, 114−121.
(52) Wang, H.; Kline, D. J.; Zachariah, M. R. In-Operando High-Speed Microscopy and Thermometry of Reaction Propagation and Sintering in a Nanocomposite. *Nat. Commun.* **2019**, *10*, No. 3032.
(53) Jacob, R. J.; Kline, D. J.; Zachariah, M. R. High Speed 2-Dimensional Temperature Measurements of Nanothermite Composites: Probing Thermal Vs. Gas Generation Effects. *J. Appl. Phys.* **2018**, *123*, No. 115902.
(54) Kline, D. J.; Rehwoldt, M. C.; Wang, H.; Eckman, N. E.; Zachariah, M. R. Why does Adding a Poor Thermal Conductor Increase Propagation Rate in Solid Propellants? *Appl. Phys. Lett.* **2019**, *115*, No. 114101.
(55) Mukasyan, A. S.; Rogachev, A. S. Discrete reaction waves: Gasless combustion of solid powder mixtures. *Prog. Energy Combust. Sci.* **2008**, *34*, 377−416.
(56) Egan, G. C.; Zachariah, M. R. Commentary on the Heat Transfer Mechanisms Controlling Propagation in Nanothermites. *Combust. Flame* **2015**, *162*, 2959−2961.
(57) Sullivan, K. T.; Zhu, C.; Duoss, E. B.; Gash, A. E.; Kolesky, D. B.; Kuntz, J. D.; Lewis, J. A.; Spadaccini, C. M. Controlling Material Reactivity using Architecture. *Adv. Mater.* **2016**, *28*, 1934−1939.
(58) Hermance, C. E. A Model of composite Propellant Combustion including Surface Heterogeneity and Heat Generation. *AIAA J.* **1966**, *4*, 1629−1637.
(59) Mallard, E.; Le Chatelier, H. L. Thermal model for flame propagation. *Ann. Mines* **1883**, *4*, 379−568.
(60) DeLisio, J. B.; Yi, F.; LaVan, D. A.; Zachariah, M. R. High Heating Rate Reaction Dynamics of Al/CuO Nanolaminates by Nanocalorimetry-Coupled Time-of-Flight Mass Spectrometry. *J. Phys. Chem. C* **2017**, *121*, 2771−2777.
(61) Rogachev, A. S. Exothermic Reaction Waves in Multilayer Nanofilms. *Russ. Chem. Rev.* **2008**, *77*, 21.

https://dx.doi.org/10.1021/acs.jpcc.0c01647
J. Phys. Chem. C 2020, 124, 13679−13687